ECN Spray D visualization of the spray interaction with a transparent wall under engine-like conditions. Part II: Impinging spray combustion.

Jesús E. Peraza[a], Raul Payri[b], Jaime Gimeno[b,*], Pedro Martí-Aldaraví[b]

[a]*FEV Iberia SL, World Trade Center Barcelona, 08039 Barcelona, Spain.*
[b]*CMT - Motores Térmicos, Universitat Politècnica de València, 46022, Valencia, Spain.*

*Corresponding author. E-mail address: jaigigar@mot.upv.es.

Abstract

In spite of the ever more comprehensive studies on diesel combustion, there is still an important gap on the fundamental knowledge about the interaction of fuel sprays with the piston and cylinder walls in internal combustion engines. The present research corresponds to the second part of an extensive investigation about the spray/wall impingement process at engine-like conditions and its sensitivity to several operating conditions. A constant pressure-flow test rig, which was filled with air extracted from the environment, was employed to perform the experiments at reactive conditions. A single-hole injector from the Engine Combustion Network, referred to as Spray D was employed and a quartz flat wall was set in front of the nozzle by using a supporting structure attached to the vessel. Parameters varied in this work are injected fuel, ambient density, gas temperature, injection pressure, and wall position in terms of distance from the injector hole and inclination angle. Three cameras were simultaneously used to observe the spray-wall interaction (SWI): Schlieren visualization to record the macroscopic evolution of the spray vapor phase and also to determine the ignition delay, a high-speed camera was placed in the front of the wall to directly observe the natural luminosity of the flame through the transparent wall and, finally an intensified camera was used to determine the lift-off length by observing the chemiluminescence of OH*. An extensive geometrical characterization of the spray geometry evolution was made and different metrics were introduced in this work as it is the case of wall lift-off radius to parametrize the observed formation of a lift-off area onto the wall. Similarly, ignition delay showed to be shortened by the presence of the quartz wall up to 15% due to its nearly isothermal configuration and its improvement on air-fuel mixing.

Keywords: Combustion, Spray-wall interaction, Post-impingement characteristics, Schlieren imaging, Natural luminosity, Ignition delay, Lift-off length, Engine Combustion Network

1. Introduction

The international community has focused efforts on the reduction of pollutant emissions produced by human activities, creating environmental regulations which are ever more challenging to fulfill. A field of special interest in this context is the one related to the internal combustion engines (ICEs) that are widely used for transportation, energy generation and industrial application [1–3]. Although plenty of research has been carried out about injection-combustion topics and many technological innovations have been accomplished for diesel ICEs, the phenomena involved in the interaction of the fuel jet with a wall when the spray impinges on it is not fully understood yet [4–6]. The trend of engine manufacturers of designing ever smaller sized direct-injection diesel engines, where spray-wall interaction (SWI) is more prone to occur due to the shorter distances between the injector nozzle and the chamber and piston walls, makes this topic a more serious issue. The deposition of a fuel film on the walls promotes the formation of unburned hydrocarbons (UHC) along with thermal energy losses because of the heat transmitted through the wall, affecting both the emissions limiting capacity and the efficiency of the engine. On the contrary, the SWI is expected to improve the gas-fuel mixing inside the combustion chamber, due to the secondary atomization and the better distribution of the spray [7, 8]. Both aspects, and the high transitoriness of this phenomenon whose temporal scale is in the order of milliseconds, make SWI a process whose analysis is quite defiant.

Cite as:
Peraza, J.E., Payri, R., Gimeno, J., Martí-Aldaraví, P., "ECN Spray D visualization of the spray interaction with a transparent wall under engine-like conditions, Part II: Impinging spray combustion", *Fuel* (2022), Vol. 308, 121964, doi: https://doi.org/10.1016/j.fuel.2021.121964

Nomenclature

Acronyms	
ASOE	After start of energizing
ASOI	After start of injection
CMOS	Complementary metal-oxide-semiconductor
CPF	Constant-pressure flow (facility)
DBI	Diffused backlight illumination
D2	Diesel #2 (abbr. used in plot legends)
ECN	Engine Combustion Network
EGR	Exhaust gases recirculation
ICCD	Intensified charge-Coupled Device
k-factor	Conicity factor used in industry
NL	Natural luminosity
nC12	n-Dodecane (abbr. used in plot legends)
SWI	Spray-wall interaction

Variables	
C	Coefficients of discharge (defined by subscript)
D	Diameter
d	Distance
k-factor	Conicity factor used in industry
ID	Ignition delay
LoL	Lift-off length
p	Pressure
R	*R-parameter*
T	Temperature
WLoR	Wall lift-off radius
X	Horizontal spray spreading
Y	Upwards spray spreading
Z	Spray thickness or height

Greek Symbols	
Δp	$p_{rail} - p_{amb}$
ϕ	Spray angle
ρ	Density
τ	Start of SWI
θ	Angle (of the wall)

Subscripts	
$+$	Wall upwards direction
100	Total distillation (temperature)
a	Area (coefficient)
amb	Ambient condition
f	Measured from the front
o	Nozzle outlet
rail	In-rail, of injection (pressure)
thXX	Measuring point location (in mm)
w	Related to the wall

Computational Fluid Dynamics simulations represent an attractive alternative in the study of a topic of such difficult experimental approach, even more considering the huge detailed information that can be obtained from them. Naber and Reitz [9] carried out one of the first attempts to model SWI. They considered three different regimes to model the interaction between the wall and drops: Stick, where the drop remains adhered to the wall, Reflect, where drops are considered to rebound specularly and Jet, in which the incident drop leaves tangent to the surface similarly than a liquid jet. Those models were tested in the KIVA code and compared with experimental spray outlines provided by Kuniyoshi et al. [10] obtaining a reasonably good agreement. However, the model of the spray generally underestimated the measured spray contour due to the limited range of drop size considered in the simulations. Gonzalez et al. [11] adapted this model to better fit the experimental data [12] at cold-starting diesel conditions. Eulerian-Lagrangian approaches have been employed [13, 14] finding that splashing is improved by changing the impact angle of the drops. Several works [15, 16] have pursued the simulation of the interaction of drops with wetted and dry surfaces and the effect of the heat transfer on atomization has been taken into account in the models used in [12, 17, 18]. Nevertheless, a particularly difficult issue is the inclusion of the effects of surface physical properties [19].

Unfortunately, the improvement of CFD models comes hand in hand with the existence and use of experimental data of high quality and reliability. Experiments that have been carried out encompass a large frame of approaches such as the study of droplets [7, 19, 20] and, in a more scanty way, sprays (multiple drops interacting with the environmental gas, the wall and between them) [21, 22]. Another variable that has to be considered is the conditions of the ambient where the fuel is injected. Akop et al. [23] performed a study in an ambient at atmospheric pressure, while a constant-volume vessel was set at $4.2\,\mathrm{MPa}$ and $1000\,\mathrm{K}$ by López and Pickett in [24] with the purpose of analyzing the effect of SWI on soot formation. Those aforementioned experiments were carried out injecting fuel on a flat wall. Another approximation employed by Pickett and López in another research [6] was to confine the jet inside a flat wall and transparent side walls in order to simulate a piston bowl for a typical heavy-duty combustion chamber near top dead center. However, the more the experiment resembles real diesel in-cylinder conditions, the more difficult is to discuss the individual effect of a determined parameter on SWI. For that reason, less realistic situations are often used to insulate the studied phenomenon [25, 7, 23, 26].

This experimental work contemplates an intermediate approach to the diesel engine-like conditions, employing a quartz flat wall to study the SWI process in a high-temperature and high-pressure ambient. A wide range of operating conditions were set in a constant-pressure flow (CPF) facility, where the wall was located at different inclination angles and distances from the nozzle exit. An experimental single-hole injector, referred to as Spray D, which was donated by Robert Bosch GmbH to the Engine Combustion Network (ECN) open forum to

which the authors belong, was employed to perform the study with two different fuels (n-dodecane and commercial diesel). This manuscript is part of a larger investigation which studies the spray-wall interaction both at inert conditions and at reactive ones by changing the ambient gas between N_2 and O_2 respectively. This paper covers the reactive part of the research, where combustion indicators such as lift-off length and ignition delay are measured together with macroscopic characteristics of the reactive spray when it spreads along the wall. Three imaging methodologies were used simultaneously: Schlieren to observe the vapor phase of the spray, OH* chemiluminescence and natural luminosity. The last has been used to have a frontal view of the impinging flame through the transparent wall.

The paper is structured as follows: right after this introduction, the experimental test rig, the optical setup and the processing routines are described. After that, results are presented and analyzed. Finally, the conclusions section summarizes the most important findings of this work.

2. Materials and methods

2.1. Hardware

2.1.1. Visualization test rig

The high-pressure and high-temperature test chamber (hPhTC) shown in Figure 1-left, was used to perform the experiments. The ambient gas, initially stored in reservoirs from a compressor, is introduced into the test rig through a $30\,\mathrm{kW}$ electric heaters system that is in the bottom of the vessel in order to control ambient gas temperature. After the gas is exhausted from the chamber, it is cooled down and recirculated to the compressor again or thrown to the atmosphere depending on the desired concentration of oxygen [27, 25]. In this experiment, the air is introduced from the atmosphere in an open loop configuration in order to have a standard air oxygen concentration around 21%. The control system is a closed loop PID, where both the pressure in chamber and the heaters output power (and therefore, in-chamber conditions of temperature and density) are controlled. The vessel has a double wall configuration in order to improve the temperature homogeneity within the chamber and reduce thermal losses. The outer wall has a purely structural function, and it is separated from the inner one by a thick insulating layer. This facility, is not only able to operate at conditions up to $950\,\mathrm{K}$ and $13\,\mathrm{MPa}$, but also has the singular feature of provide nearly quiescent and steady thermodynamic conditions, which allows to perform wide-range test matrices with multiple repetitions in short testing periods and grants a better reproduction of real engine-like conditions. The chemical composition of the ambient gas in the chamber is continously monitored by a lambda sensor [27, 28].

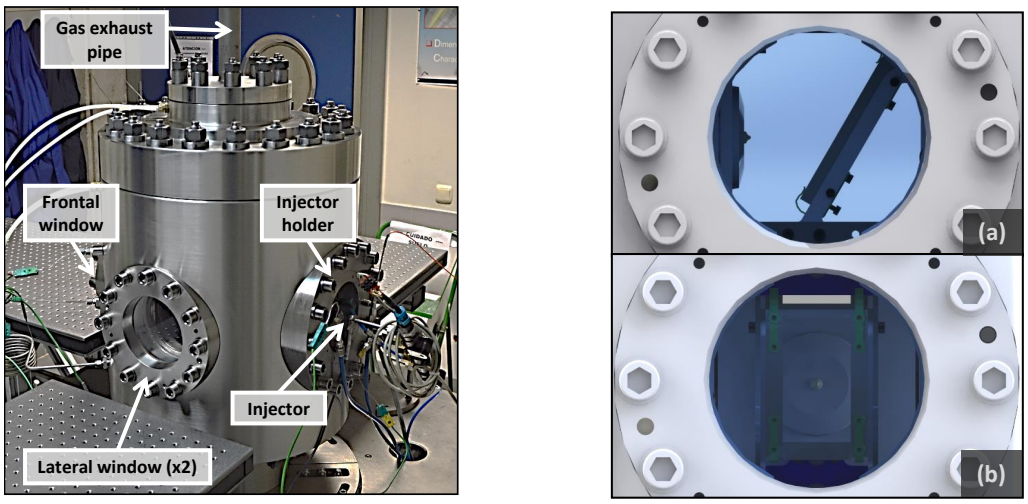

Figure 1: High-pressure and high-temperature vessel. Left: Test rig photograph. Right (a): Field of view of the lateral window. Right (b): Field of view of the frontal window (d_w = 50 mm; θ_w = 60°)

The hPhTC has three orthogonally-placed windows that are used for optical access. Those windows are

128 mm diameter, providing the field of view that is shown in Figure 1-right (a) from the lateral ones and Figure 1-right (b) from the frontal one. In the images, the wall is shown in a configuration of d_w = 50 mm and θ_w = 60°, considering those values the distance between the wall and the injector tip and the angle of the wall respect to the horizontal plane.

2.1.2. *Injection system*

The injector used for the experiments is the ECN Spray D axial single-hole injector (serial #209135), which is one of the target injection hardwares of the Engine Combustion Network [29–31]. It has a convergent nozzle (with a *k-factor* of 1.5) that is provided with a rounded inlet in order to avoid cavitation to occur. This mono-orifice injector has a nozzle outlet diameter of 192 µm and has been hydraulically characterized by Payri et al. [32]. Several geometrical characteristics of the nozzle can also be found on the ECN database [29]. Finally, this injector is used with n-dodecane (nC12) and diesel #2 (D2) as indicated in Table 1, in order to analyze the effect of fuel properties on reacting SWI.

2.1.3. *Quartz wall system*

A transparent JGS1 quartz block (100×60 mm^2 surface and 10 mm depth) has been used as subject for spray-wall interaction. This has been possible by the use of the supporting system shown in Figure 2 [25]. An injector cap is placed as a layer between the hot ambient and the injector body, and it has been painted in matte black to prevent reflection of the light emitted by the flame. Two folded sheets are screwed to this injector cap in order to hold two 'U' shaped structures that hold the wall in different positions. The position of the wall in terms of distance respect to the injector tip (d_w) and inclination angle (θ_w) is controlled by using different exchangeable frames (shown in green in Figure 2-left), that come in pairs with different shapes to set different conditions with good accuracy. The frames are attached to the wall holder that is pressed against the wall by the use of four adjustable hooks.

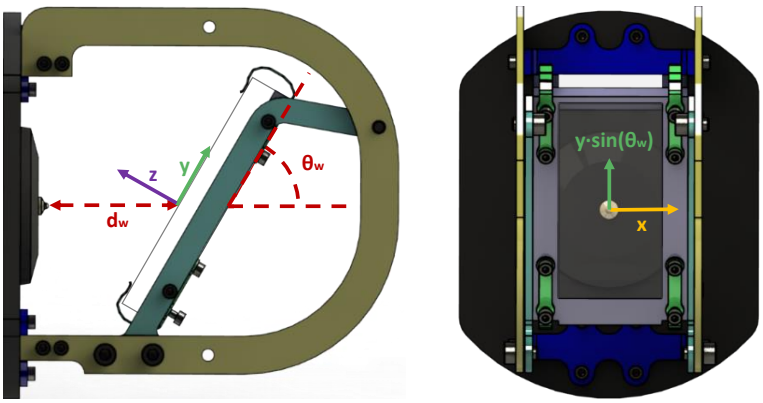

Figure 2: Wall support system. Left: Lateral view. Right: Frontal view

2.2. *Test plan*

A wide range of conditions has been included in the test matrix for this study, which can be seen in Table 2. Most of them are target conditions of the ECN group[29], while some others are used in order to cover a larger spectrum. Particularly, six different combinations of wall positions have been used, along with the two fuels previously described. Injection pressure, ambient temperature and density were also changed within a range of diesel-like real conditions. Ten repetitions have been performed in each test condition. Additionally, injection frequency has been configured to 0.25 Hz, after experimental evaluation to ensure rep-to-rep control and repeatability of boundary conditions.

Table 1: Fuel properties for n-dodecane and diesel #2 [29].

Fuel Property	n-Dodecane	Diesel	Units
T_{100}	489	623	K
Cetane number	87	46	-
Lower heat value	44.17	42.975	MJ/kg
Fuel density[1]	752.1	843	kg/m^3
Aromatics concent.	0	27	%
H_2 mass concent.	15.3	13.28	%
Kin. viscosity[2]	1.5	2.35	mm^2/s
Flash point	356	346	K
Sulfur content	0	9	ppm
Plot legend[3]	nC12	D2	-

[1] Value at 15 °C
[2] Value at 40 °C
[3] Name employed in plot legends due to spacing reasons

Table 2: Test conditions summary.

Parameter	Values	Units
Injector	Bosch 3-22 Spray D	-
Fuel[a]	nC12 - D2	-
Energizing time	2.5	ms
Tip temperature	363	K
Oxygen perc. (O_2%)	20.9 (standard air)	%
Gas temperature (T_{amb})[a]	800 - 900	K
Gas density (ρ_{amb})[a]	22.8 - 35	kg/m^3
Injection pressure (p_{rail})	50 - 100 - 150 - 200[b]	MPa
Wall distance (d_w)[a]	30 - 50	mm
Wall angle (θ_w)[a]	30 - 45[c] - 60[c] - 90	°

[a] Not all possible combinations have been tested.
[b] Only for diesel tests.
[c] Only for d_w = 50 mm.

2.3. Experimental techniques

2.3.1. Optical setup

Three cameras were simultaneously used to obtain spray and/or flame images from different approaches and purposes, employing the optical arrangement shown in Figure 3, where the main light paths of the different techniques are shown in dashed lines of different colors. Schlieren imaging (blue) has been used for the visualization of the vapor phase of the spray and the burned gases produced in combustion. OH* chemiluminescence (green) has been employed in order to estimate the flame lift-off length location by observing the light emitted by the OH* radicals while decay to their ground state. Finally, a high-speed camera is located in front of the vessel to directly observe the flame spreading onto the wall through natural luminosity (NL) diagnostics (red).

In the case of Schlieren imaging, a continuous Xe-Arc lamp that is connected to an optical fiber ends in the point light source seen in the scheme. Then, light travels to a parabolic mirror that collimates the rays that go through the chamber. Those rays are collected by a biconvex lens that makes them converge to the Photron SA-X2 camera. In the chamber, density gradients affect refraction index and deviate the rays from their parallel original path, making those deviated beams not to reach the camera due to the narrow diaphragm gap.

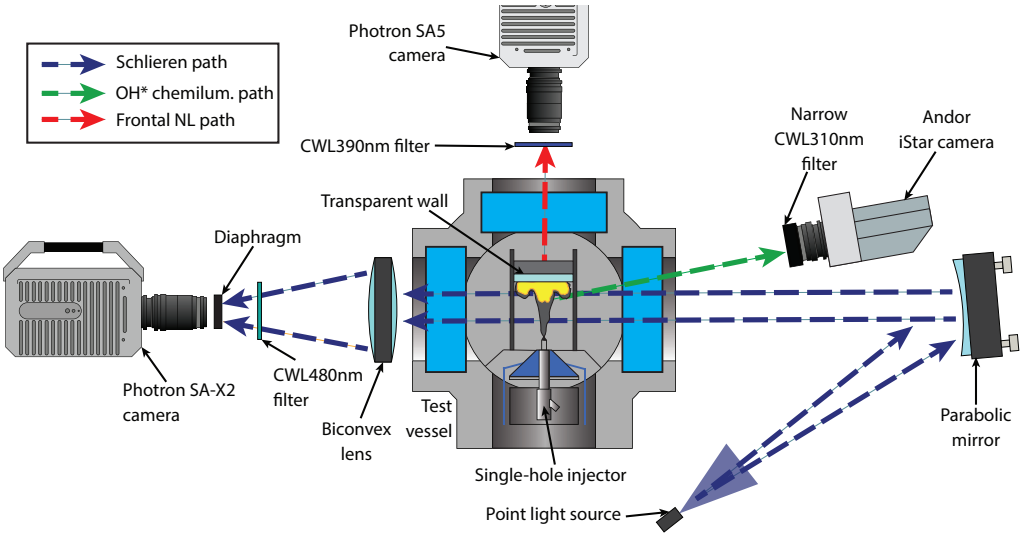

Figure 3: Optical setup employed in the experiments. Schlieren imaging, OH* chemiluminescence and natural luminosity have been simultaneously used.

The frontal high-speed camera has been configured with a long exposure time in order to detect flame regions with low intensity and precursor chemical reactions at the beginning of the exothermic processes that lead to combustion, however, a bandpass filter has been used in order to avoid image saturation. Finally, an ICCD Andor iStar camera, fitted with a 100 mm f/2.8 UV lens and a 310 $\pm$ 5 nm CWL filter was employed to capture a single

image per injection event. This image is taken only in a time gap during the steady part of the combustion, in order to avoid deviations. The ICCD camera has been inclined 6° not to obstacle the Schlieren arrangement and this inclination has been corrected afterwards via image processing. More details about the setup of the optical arrangement can be found in Table 3.

Table 3: Details of the optical setup for the employed techniques.

	Camera	Sensor type	Filter CWL	Exposure time	Frame rate	Px/mm ratio
Schlieren imaging	Photron SA-X2	CMOS	480 nm	3.28 μs	40 kfps	5.88
OH* chemiluminescence	Andor-iStar	ICCD	310 nm	2.5 ms*	1 frame/inj	8.82
Frontal NL	Photron SA5	CMOS	390 nm	19.25 μs	25 kfps	9.60

* For the ICCD camera, a TTL-delay was set from 1.5 to 3 ms (ASOE) depending on the ignition delay.

2.4. Image processing methodologies

2.4.1. Videos from high-speed cameras

Image processing is one of the most relevant parts of any data analysis extracted via visualization. Different types of images have been extracted from the different optical setups previously described and have been processed with an in purpose-developed routine in Matlab. The process is broadly the same for all the movies from high-speed cameras. Nevertheless, a preprocessing step defines the kind of image in terms of the optical technique in order to classify them by background type (dynamic-static, dark-illuminated, etc.).

The strategy consists basically on defining the background of image and subtracting it from all the images, to normalize its luminosity levels. Background is considered to be static in natural luminosity images and is taken by averaging a determined number of images before the start of injection (this number is dependent of camera frame rate). In Schlieren imaging, the background is calculated for each image as it is considered as dynamic (with variations that are noticeable, but significantly slower than spray evolution). Schlieren contour calculation is based on the independent use of two criteria that are finally combined to obtain a single binarized image where white is "spray" and black is "background": the first one, the only one used for NL images, is based on the use of a fixed threshold on the intensity levels of the images, and the second one is based on the study of the standard deviation of two consecutive images in order to detect variations on spray pixels that are stronger than the ones of the background. The images obtained with each criterion are filtered via morphological operations in order to prevent background irregularities, then they are combined in a weighted average, obtaining the final spray contour. Figures 4 and 5 are some samples of the contours that are obtained with this approach for both Schlieren and NL images.

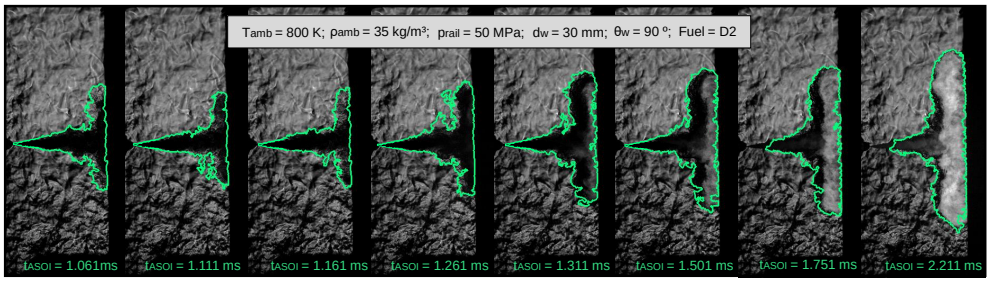

Figure 4: Series of spray images and contours of a random sample of the reacting spray recorded via Schlieren (T_{amb} = 800 K; ρ_{amb} = 35 kg m^{-3}; p_{rail} = 50 MPa; d_w = 30 mm; θ_w = 90°; Fuel = D2).

The contours obtained with the aforementioned approach are used to calculate different variables. Figure 6 shows how spray spreading (Y_+) and spray thickness (Z_{th}) are defined, the latter measured at three different distances (10 mm; 20 mm and 30 mm) from the "collision point" or the interception between the spray axis and the wall plane. Additionally, the derivative of spreading respect to the square root of time ($\partial Y_+/\partial\sqrt{t}$) has been calculated and reported under the name of *R-parameter* (R_Y). This derivative has shown in different researches

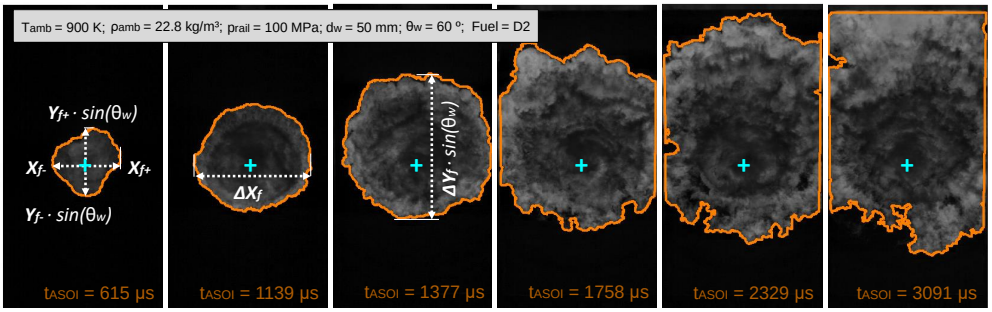

Figure 5: Sequence of the flame spreading event observed through the transparent wall. (T_{amb} = 900 K; ρ_{amb} = 22.8 kg m^{-3}; p_{rail} = 100 MPa; d_w = 50 mm; θ_w = 60°; Fuel = D2).

to be useful to study both free penetration and spray-wall spreading, and to establish analogies between them regardless of the temporal reference [27, 25, 33] at inert cases or to define the behavior of the reacting spray evolution [3].

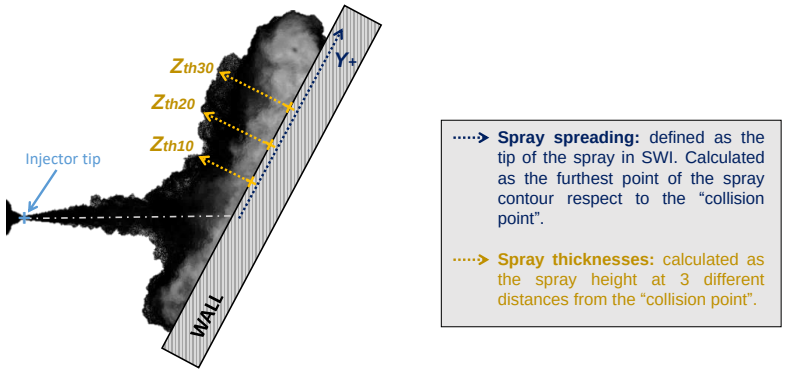

Figure 6: Indication of the geometrical features that are obtained from the Schlieren images.

On the other side, the parameters that are measured from the frontal natural luminosity images are shown in the three first frames of Figure 5. First, frontal flame spreading is measured vertically (Y_{f+} and Y_{f-}) both downwards and upwards and applying the correction of the wall inclination angle. Flame spreading is also measured horizontally in both left and right directions (X_{f+} and X_{f-}). Finally, the flame width in both horizontal and vertical orientation (ΔY_f and ΔX_f) are computed too as the sum of two spreadings in opposite direction.

Different temporal variables are also calculated taking advantage of the high temporal resolution of the Photron CMOS cameras. Specifically, the start of spray-wall interaction (τ_w) and ignition delay (*ID*) were parameters of special interest in this work and were calculated from the Schlieren images. τ_w is obtained from free penetration as the time when it equals d_w. Nevertheless, to prevent a misdetection of this time due to dark pixels from background near from the wall, numerical gridded fit is created from penetration data. This fit is then extrapolated to d_w and the time when they match is taken as τ_w. This methodology is explained more in detail in the inert part of this research [33].

Schlieren imaging is also used for ignition delay calculation. Two different ignition delays can be observed from those images: the first stage of ignition, also known as start of cool flames (SoCF), when the first indications of chemical reactions occur and the head of the diesel spray adopts a refractive index similar to the one of the hot air of the ambient [28], and the second stage of ignition (SSI), where high-temperature reactions take place and the spray presents incandescent flames and rapid expansion. An intensity-based strategy that is extensively used in free diesel sprays [34, 3] has been employed in this paper to calculate the second stage of ignition, which is hereinafter the reported *ID*. The pixel-by-pixel intensity into the detected spray contour is calculated frame by frame. It is totalized as plotted in Figure 7-top and then derived to obtain the intensity increment as a time resolved signal, shown in Figure 7-bottom, where the different repetitions are shown in dots and the polynomial-averaged curve is shown in black lines. The local maximum of the intensity increment (intensity derivative) is taken as *ID*.

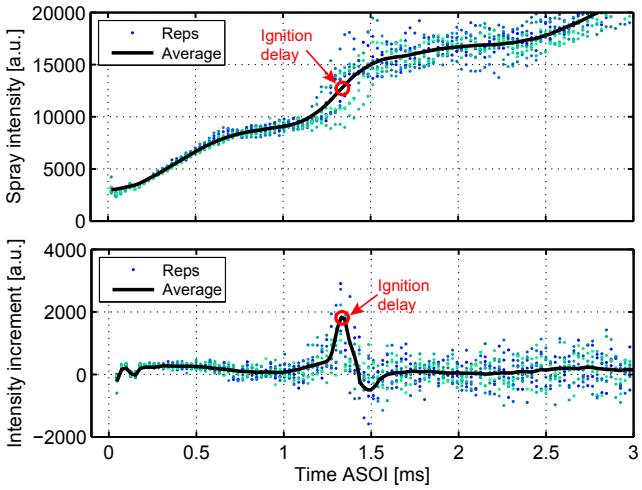

Figure 7: Principle of calculation of ignition delay based on the evolution of the spray intensity and its derivative. Top: Spray intensity raw data per rep and averaged. Bottom: Spray intensity variation at the same conditions

2.4.2. OH chemiluminescence images*

For lift-off length (*LoL*) calculation, OH* chemiluminescence images have been processed following a strategy based on the methodology employed by Gimeno et al. in [35]. A raw image (consider the sample in Figure 8-left) is taken and a fixed threshold of 0.3 between the 5% and 95% of the max intensity level is used to mask the image, covering the pixels below this value (Figure 8-right). Then, the flame is divided into two bottom and top halves and a fixed radial distance in the detected flame is used for the two halves of the image to define a region of interest. The location of the corrected leftmost pixel above the 50% of the max intensity level in this region is considered as lift-off length. Finally, the reported *LoL* is obtained by averaging the calculated in the two halves and also all the respective repetitions of the targeted test.

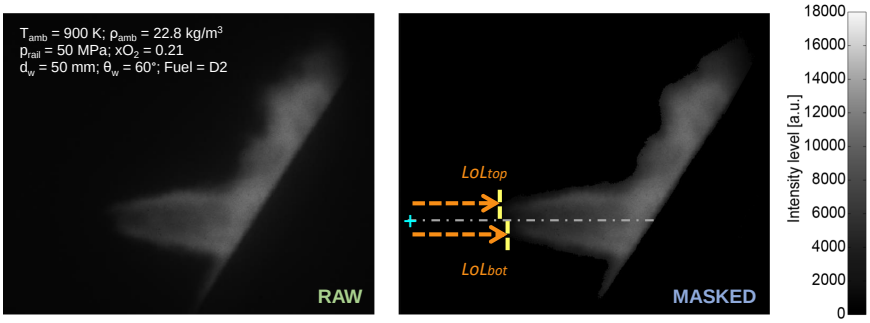

Figure 8: OH* imaging sample and variables calculation. Left: Raw image. Right: Image after being masked from binarization results.

3. Results and discussion

3.1. Ignition delay

Ignition delay is defined as the time elapsed from start of injection to the start of high-temperature reactions that lead to the air-fuel mixture combustion [36, 37]. Figure 9 depicts ignition delay for different conditions. The left set of plots shows different operating conditions while the right one illustrates different fuels and wall positions. As it could be expected from free-jet literature, ignition delay is strongly shortened by ambient temperature as main factor. In the case of the target conditions of this study, *ID* shortenings close to 60 % are observed from

800 K to 900 K. Density promotes an enhancement on the mixing process and a larger oxygen availability and injection pressure increments the turbulence level, both representing in a lesser extent (between 17 % and 30 %) a reduction on ignition delay. All the effects get less relevant for short ignition delays.

The right set of Figure 9 shows the dependence of ignition delay on wall conditions and fuel properties, including the no-wall case. The high volatility of dodecane respect to diesel #2, shown in the first part of this work [33] in terms of liquid phase behavior, makes it prone to ignite before. This observation is in accordance with the results and with the cetane indexes shown in Table 1, being nC12 cetane number approximately two times the diesel one. Wall angle does not seem to have a significant effect on ignition delay. By previously observing that the smaller the wall angle, the larger the stable liquid spreading, it could lead to think that ignition delay should diminish with angle increase. However, rather than an improvement in the evaporation process due to a better atomization, this happens solely by the jet deviation on the wall that, when it is inclined, has a preferential direction while in a perpendicular wall the liquid spreads in all directions. To confirm it, an adequate further analysis could be computation of the liquid volume of a spray that impinges onto an inclined wall, as done for the θ_w = 90° wall, by the use of a different optical technique. With regard to the droplet break-up caused by the wall, it does not present significant changes with collision angle, but its presence definitively makes a difference respect to the free-jet case, where the lack of this secondary break-up (and of its consequent increment on local turbulence levels) induced by the beginning of SWI delays the ignition.

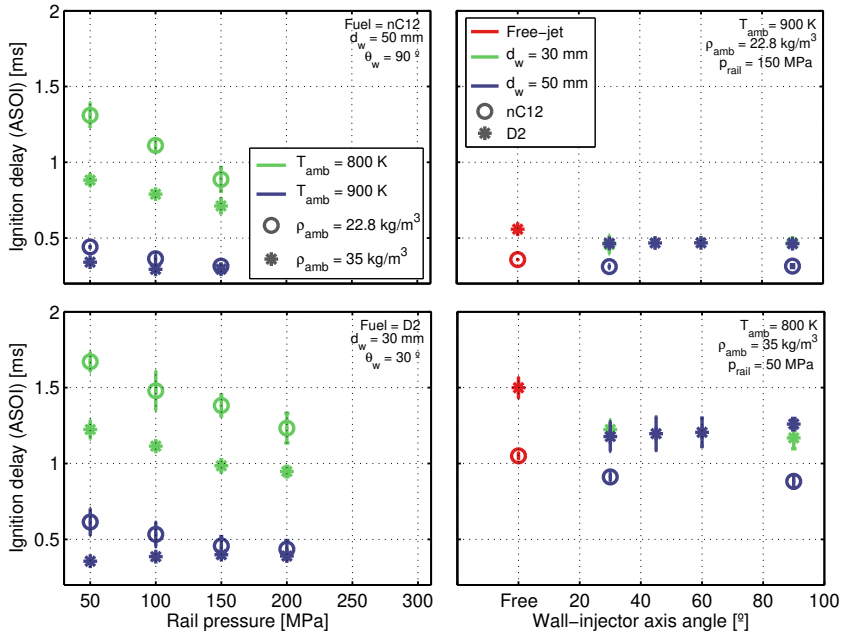

Figure 9: Ignition delay calculated for different conditions. Left set: *ID* vs injection pressure varying ambient temperature and density. Right set: Variation of ignition delay vs. wall angle at different wall orientations and fuels (free-jet included).

This is better observed in Figure 10, where *ID* is plotted for all the points with SWI (Y-axis) against points at the same operating conditions but with no wall in the chamber (X-axis). The two plots gather the same points with different variables used to identify them by color, marker, etc. It can be seen that short ignition delays are quite similar in both cases since they take place before the spray reaches the wall, in other words, with no SWI or a very short proportion of SWI in the mixing process before ignition delay. As ignition delay gets longer, it starts to be affected by the wall due to the acceleration in the reactions produced by the mixing and turbulence improvement reaching reductions up to 15 %. Furthermore, *ID* is consistently shorter for d_w = 30 mm because of the earlier impact between the spray and the wall.

3.2. Reacting spray-wall interaction via Schlieren

Schlieren visualization has been performed to obtain the spray morphology evolution in its vapor phase. The use of this approach implies that the detected spray covers both the vapor phase of the fuel and the gaseous burned

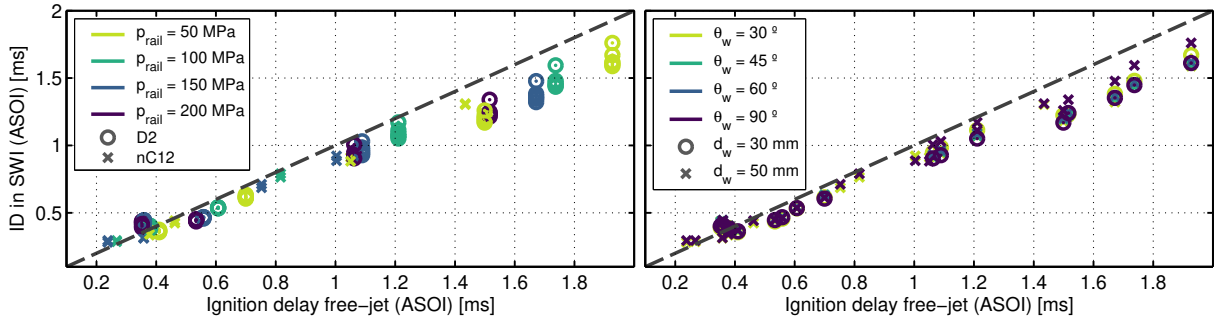

Figure 10: Ignition delay with the quartz wall in SWI conditions vs. ignition delay at free-jet conditions. The gray dashed line represents $ID_{free\text{-}jet} = ID_{SWI}$. Both plots have the same information differently classified. Left: Fuel and injection pressure variation. Right: Changes in wall position.

products of combustion that are similarly part of the spray. The behavior of the spray covered by this definition is what is reported and hereafter referred to as "vapor". Figure 11 shows spray spreading onto the wall for both reacting and inert conditions by changing oxygen concentration (the inert tests points were extracted from [33]). The top plots show spreading for different ambient temperatures and the bottom plots illustrate the behavior of R_Y for the same conditions. The plots are temporally referenced after the start of SWI and ignition delay (under this reference) is identified with a circular marker. Therefore, if it is not in the plot it is because ignition did not occur (inert cases) or it happened before impacting the wall (high reactivity points). The first thing that can be noticed is how spreading is larger for the reacting spray due to the combustion-driven expansion respect to the inert case. Ignition close or before the spray reaches the wall changes the initial conditions of the observed spreading, but its growth is still faster for the reacting spray. *R-parameter* analysis shows an indicator of the spray momentum [27] and is in agreement with the observations made in [27, 3] for both inert and reacting free-sprays respectively: *R-parameter* is constant with time for the steady part of the spray at inert conditions. On the other side, after ignition, there is a "bump" on spreading caused by the spray sudden expansion, then it decelerates resulting into a "valley" in the R_Y curve. Finally, R_Y rises and reaches a higher value than the one exhibited by the inert spray, in accordance with the larger spreading velocity of the cases with an oxygen concentration of 20.9%.

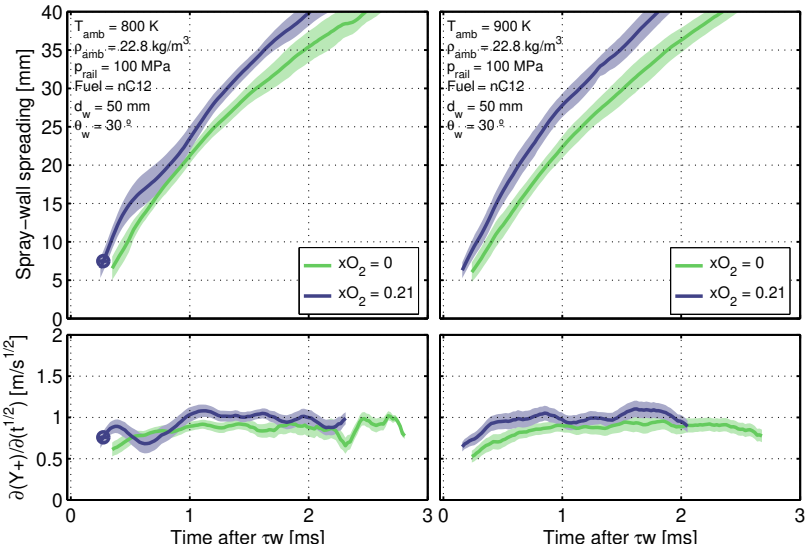

Figure 11: Spray spreading along the wall (top) an its *R-parameter* (bottom) for both reacting and inert conditions (different oxygen concentrations) and gas temperatures (ρ_{amb} = 22.8 kg m^{-3}; p_{rail} = 100 MPa; d_w = 50 mm; θ_w = 30°; Fuel = nC12). Left: Test conditions at T_{amb} = 800 K. Right: Gas temperature T_{amb} = 900 K

Figure 12 depicts the effect of rail pressure and ambient temperature. Ignition delay is reduced by an increase on injection pressure. Nevertheless, τ_w is shortened too, so in this particular case, ignition delays and *R-parameter*

bumps seem to be phased under this "after τ_w" reference. Spray momentum is proportional to *R-parameter* and increases with injection pressure. On the other hand, ambient temperature have a noticeable effect on spray spreading. Inert results [25, 33] discard important effects of temperature as a product of the aerodynamic interaction between the spray and the atmosphere. The large effect of ambient temperature on ignition delay in terms of timing and then, on how premixed is the air-fuel mixture before ignition is the factor that drives differences on spray expansion between T_{amb} = 800 K and T_{amb} = 900 K. This is specially observed in the plots of Figure 12, where the points in the left ones have ignition onto the wall and the right set shows sprays with ignition before SWI.

On the other side, Figure 13 illustrates the effect of fuel properties and air density. As expected, the spray is faster for low gas densities despite the consequent increment on ignition delay, due to the variation in the air entrainment rate. The effect of fuel physical properties in the case of diesel and dodecane seem to be negligible in comparison to the one produced by the differences on ignition delay (in regards of fuel reactivity), which causes a slight difference in stable conditions and a possible overlapping in transient stages that are out of phase due to the ignition delay gaps.

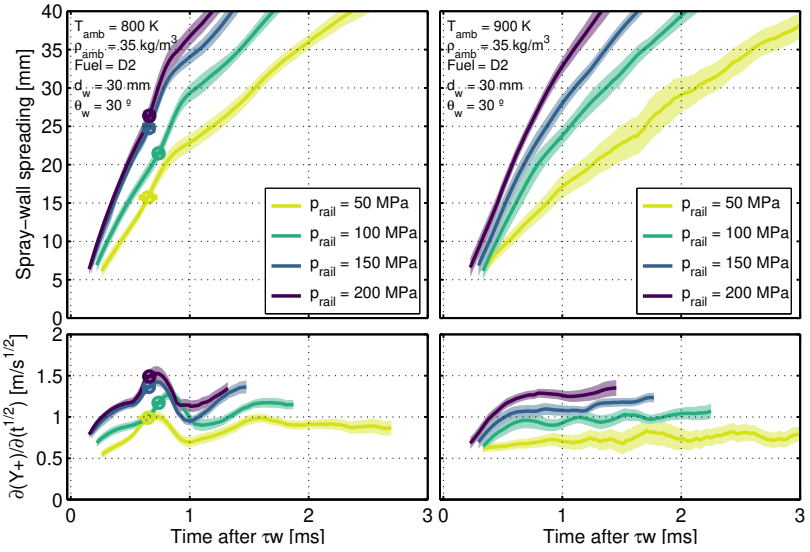

Figure 12: Reacting spray spreading (top) and its respective *R-parameter* (bottom) for different injection pressures and ambient temperatures (ρ_{amb} = 35 kg m^{-3}; d_w = 30 mm; θ_w = 30°; Fuel = D2). Left: Air temperature at 800 K. Right: Vessel set at T_{amb} = 900 K

Spray-wall spreading at different wall distances and angles is shown in Figure 14. Spreading curves at $\theta_w = 90°$ start with an apparent initial value while inclined walls depict a smoother beginning due to the already present spray width, whose projection is more significant in the perpendicular wall, and specially for those sprays that have ignited and whose width has been expanded by the combustion. Furthermore, the effect of the angle is clear: the distribution of spray momentum after the impact is not homogeneous in all directions of the wall, being more relevant in the direction of the least deviation. This direction is always upwards the wall, which is the one in which spreading is measured. The most homogeneous case is the perpendicular wall, while spreading gets faster for more inclined configurations. On the other hand, the only influence of wall distance on spreading is given by the relative ignition delay (or advance) respect to the start of SWI (i.e. for a d_w = 50 mm case, ignition delay is prone to occur before the spray hits the wall or at least to be less spread onto the wall). This is in agreement with [25, 33], where the effect of wall distance on spreading *R-parameter* is negligible at non-reacting conditions.

Regarding spray thickness, as mentioned, it has been measured at three different distances from the collision point (10 mm; 20 mm and 30 mm) observed in the three rows of plots of Figure 15, where again a direct comparison of inert [33] and reacting conditions is made. The two columns of plots are differenced in terms of having long or short ignition delay conditions (gas density and temperature), observing ignition occurring after SWI start in the case of the left graphs, and before τ_w in the right ones. In the $ID > \tau_w$ cases, spray thickness is the same for both inert and reacting atmospheres until ignition occurs. Once this happens, a strong combustion-induced expansion is observed, and it gets progressively larger as the measuring distance is further from the collision point. On the other side, the cases where $ID < \tau_w$ show a slight advancement of the reacting curve respect to the inert one due to this expansion occurred at free-jet conditions, and also a thicker spray, which means that the

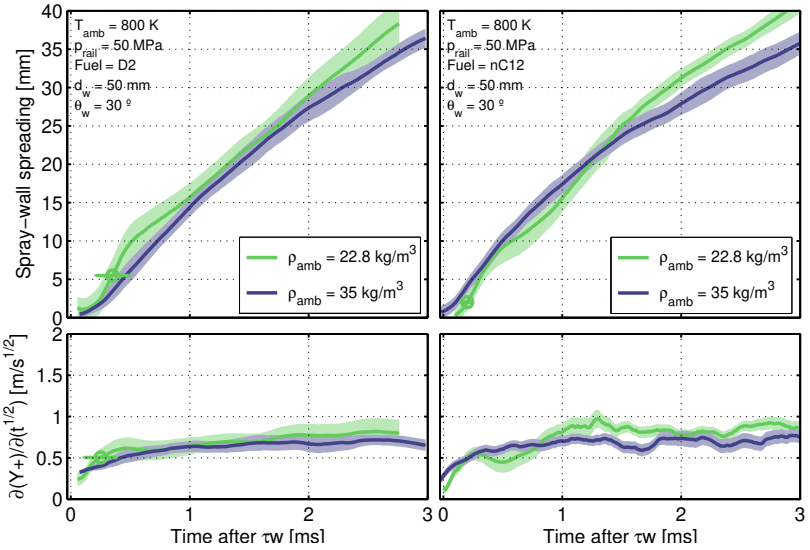

Figure 13: Reacting spray spreading (top) and its respective *R-parameter* (bottom) for different air density and fuel (T_{amb} = 800 K; p_{rail} = 50 MPa; d_w = 50 mm; θ_w = 30°). Left: Points with Fuel = D2. Right: Points using n-dodecane as fuel.

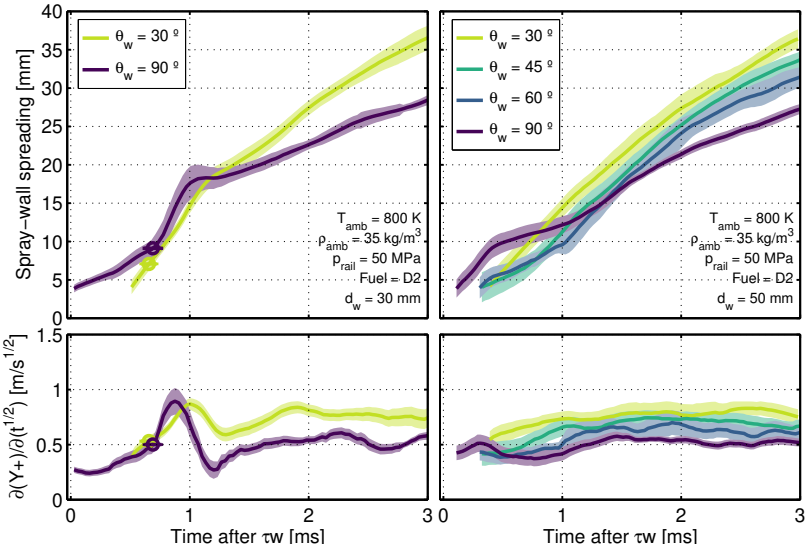

Figure 14: Reactive wall spreading (top) and their *R-parameter* (bottom) for different wall positions (T_{amb} = 800 K; ρ_{amb} = 35 kg m^{-3}; p_{rail} = 50 MPa; Fuel = D2). Left: Tests with injector-wall distance of 30 mm. Right: Wall located at 50 mm from the injector tip.

influence of this expansion on thickness is not prevented even if ignition takes place before the start of SWI.

At lower temperatures, ignition is more delayed and therefore, the air-fuel mixing process before combustion gets longer, combustion is more premixed and spray expansion shows to be stronger. This is observed in Figure 16-left, where steady thickness is narrower for the high temperature point even when its spray front reaches the measuring points before. In the right side plots, injection pressure shows a negligible influence on stable thickness in SWI since its effect on ignition timing is solid but not as strong as the case of T_{amb} and ρ_{amb}.

Air entrainment into the air-fuel mixture is incremented at high air densities, which results into a larger spray thickness, as it is illustrated in Figure 17-left. This effect, that could be expected from the knowledge of the spray angle behavior at free-jet situations and the visualization of spray-wall thickness at inert SWI conditions [38, 27, 33], is even more important than for inert sprays due to the lower density ratio ρ_f/ρ_{amb} of the products respect to the unburned fuel [39]. On the other side, the effect of changing fuels is primarily given by the difference in fuel density and it becomes more relevant due to the aforementioned reduction of density ratio after lift-off length and ignition timing gaps between fuels.

The effect of varying wall position is shown in Figure 18, where ignition delays that are shorter than τ_w were plotted since *ID* remains the same and it is not influenced by the wall. The case with the wall placed at $50\,\mathrm{mm}$ from the injector tip has a longer time between ignition and τ_w, what is to say, more time with air entrainment in a free-jet regime with a spray partially composed by burned products with a lower density than the unburned fuel before ignition. This causes a larger thickness at large wall distances as visible in Figure 18 left set of plots. Regarding wall angle, the more perpendicular it is, the slower thickness stabilization is. Also, it has to be taken into account that the observed thicknesses, specially in the $90°$ case, are given by the very front vortex that covers the spray in its periphery, since a visualization of a transversal cut of the spray is not possible via Schlieren imaging.

3.3. Frontal flame direct visualization

As previously mentioned, flame spreading was visualized from a frontal view through the transparent wall. Figures 19; 20 and 21 show the behavior of both horizontal spreadings towards the left and the right sides of the captured image (X_{f-} and X_{f+} respectively) in the top plots, and the flame width ΔX_f in the bottom ones.

Different ambient temperatures and injection pressures are shown in Figure 19. Both leftwards and rightwards spreadings are quite symmetrical, which indicates both a good alignment of the wall arrangement and a proper homogeneity of ambient conditions in the chamber. The trends remain as observed in vapor upwards spreading: injection pressure increments spreading velocity in all wall directions. High T_{amb} makes the flames to appear and be detected sooner. However, the flame growth of the low air temperature case (more premixed spray) is more abrupt and sudden.

Figure 20 shows horizontal spreading at different densities and with the two fuels, while the effect of varying wall angle and distance is illustrated in Figure 21. Most of the effects are expected from the behavior observed for vapor upwards spreading. However, the effect of wall inclination angle is hugely reduced respect to the spreading seen from the side. In this case, the axis in which spreading is measured and the axis of rotation of the wall are the same, which makes that regardless of inclination, the horizontal projection of it is $90°$ respect to the free-jet axis, having a similar distribution of spray momentum in that direction for different wall angles. Despite of the fact the view range in the horizontal direction is limited to $40\,\mathrm{mm}$ due to the wall design, it is still enough to appreciate flame behavior before steady phase and its consistency with the results of vapor spreading.

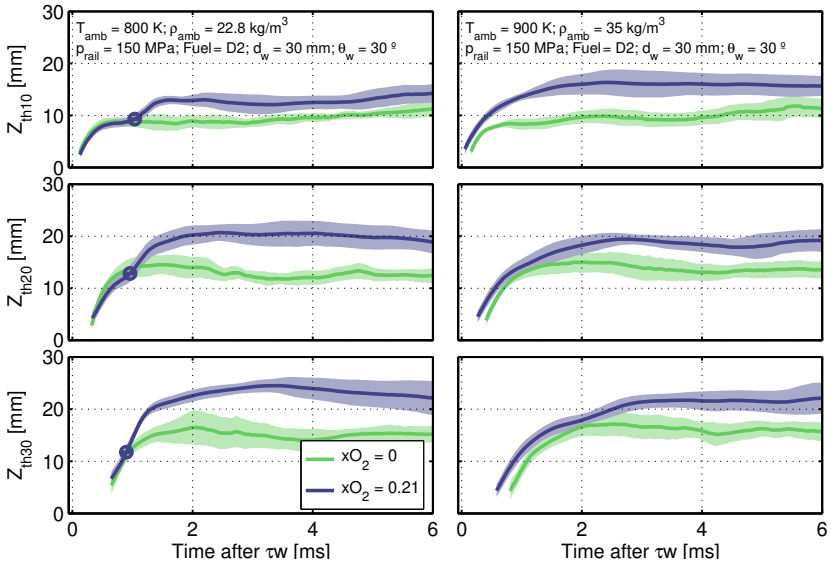

Figure 15: Spray thickness varying oxygen concentration between inert and reacting conditions (p_{rail} = 150 MPa; d_w = 30 mm; θ_w = 30°; Fuel = D2). Left: Long ignition delay conditions of gas temperature and density. Right: High temperature and density conditions (short *ID*).

.

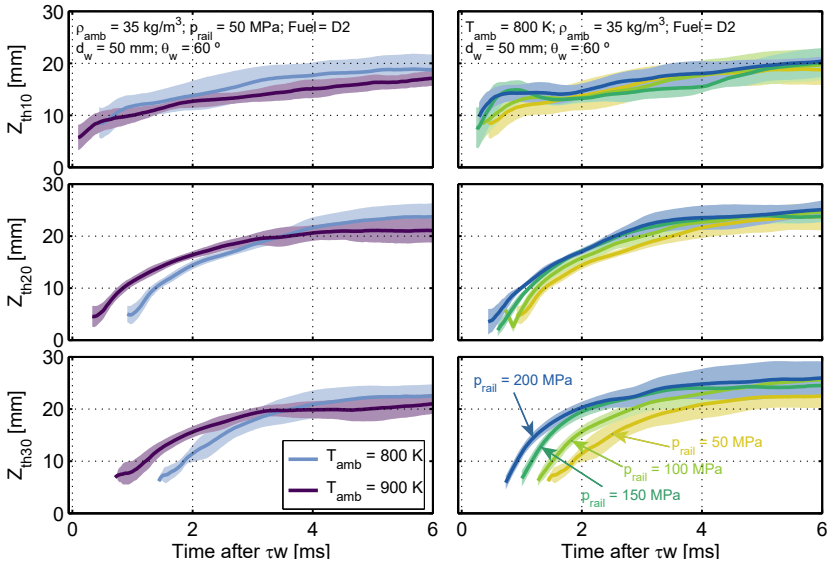

Figure 16: Spray thickness for different ambient temperatures and injection pressures (ρ_{amb} = 35 kg m^{-3}; d_w = 50 mm; θ_w = 60°; Fuel = D2). Left: Temperature variation at rail pressure of 50 MPa. Right: Different injection pressures at a fixed gas temperature of 800 K.

.

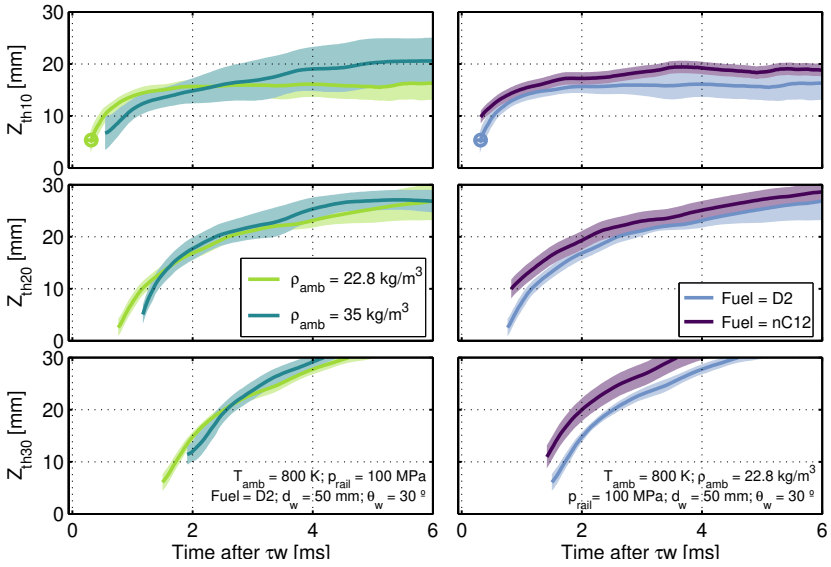

Figure 17: Spray thickness for different gas densities and fuels. (T_{amb} = 800 K; p_{rail} = 100 MPa; d_w = 50 mm; θ_w = 30°). Left: Different gas densities using diesel as fuel. Right:ρ_{amb} = 22.8 kg m^{-3} and the two fuels.

.

3.4. Lift-off length

Different optically accessible *LoLs* are shown in Figures 22 and 23. Nevertheless, lift-off lengths that tend to be large at free-jet conditions, specially taking into consideration the large diameter of the injector orifice (192 µm), are susceptible to be covered by the very thickness of the flame that is in interaction with the wall [40]. It similarly happens for test points with the wall located at d_w = 30 mm, considering that the observed thicknesses are normally around 15-20 mm in length. Figure 22 illustrates lift-off length for different operating conditions (left) and wall positions and fuels (right). Different authors [36, 41, 35] agree that lift-off length is strongly controlled by *ID*. From there, it can be understood that lift-off length is short for high ambient temperatures and densities. Also, as the effect of injection pressure on ignition delay is not as strong as the others, similar *ID*s

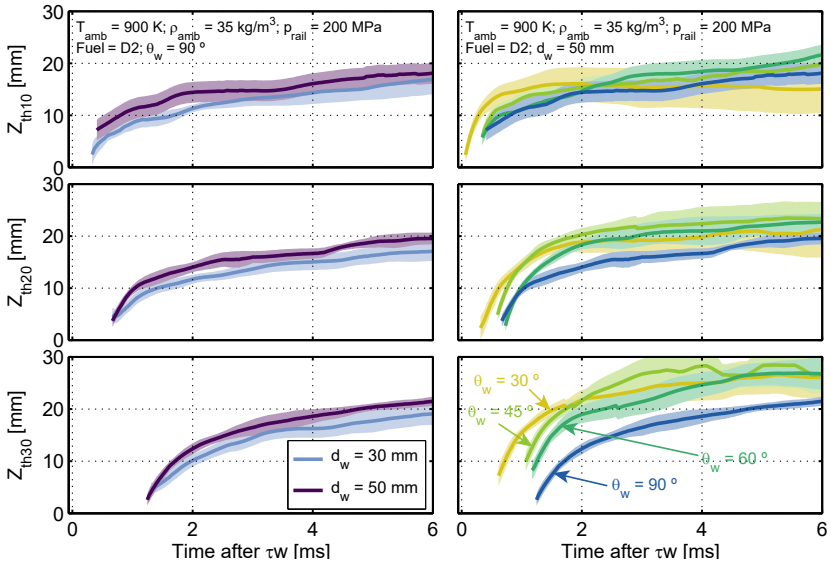

Figure 18: Spray thickness for different wall positions. (T_{amb} = 900 K; ρ_{amb} = 35 kg m^{-3}; p_{rail} = 200 MPa; Fuel = D2). Left: Different wall distances from the injector tip for θ_w = 90°. Right: Different wall angles fixing d_w = 50 mm.

.

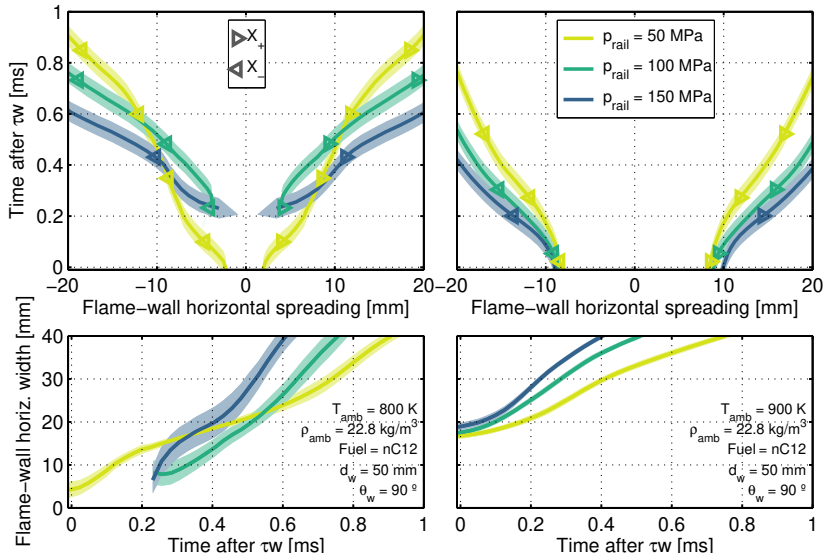

Figure 19: Flame horizontal spreadings and width for different p_{rail} (ρ_{amb} = 22.8 kg m^{-3}; d_w = 50 mm; θ_w = 90°; Fuel = nC12). Left: T_{amb} = 800 K. Right: T_{amb} = 900 K.

at higher injection pressures (spray velocities), lift-off length formates at further distances, with a nearly linear proportion. Additionally, differences in fuel reactivity affect *LoL*, which is between 10 % and 13 % shorter for nC12 compared to D2, as shown in the right side graphs.

Wall angle shows not to have apparent effect on lift-off length, and also the values shown in Figure 22-right at d_w = 50 mm have the same lift-off length than free-jet conditions (red). Unfortunately, almost all d_w = 30 mm points of the test matrix have their *LoL* covered by the very flame thickness. However, all visible *LoL*s at SWI conditions are plotted in Figure 23 compared to free-jet points at the same operating conditions, being practically unchanged for the two cases. This indicates that the quartz wall does not affect ambient conditions and it is consistent enough to consider that lift-off length is not affected by wall position, or even by the presence of the wall, at least in the range in which *LoL* is located upstream from the wall and ignition conditions are met before reaching it. In spite of several works describing a reduction on lift-off length with wall distance at high spray momentum conditions [42, 6, 43], they agree in the employment of bowl-like wall geometries and conclude

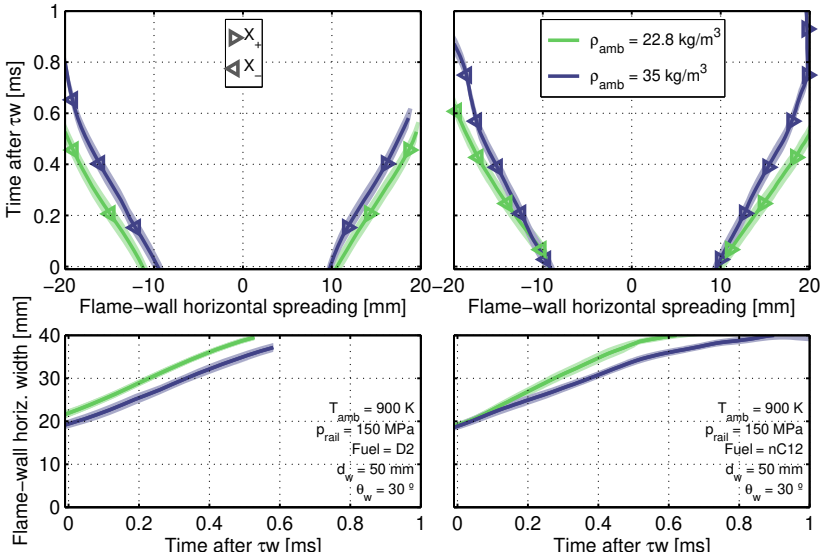

Figure 20: Flame horizontal spreadings and width for different ρ_{amb} (T_{amb} = 900 K; p_{rail} = 150 MPa; d_w = 50 mm; θ_w = 30°). Left: Fuel = D2. Right: Fuel = nC12.

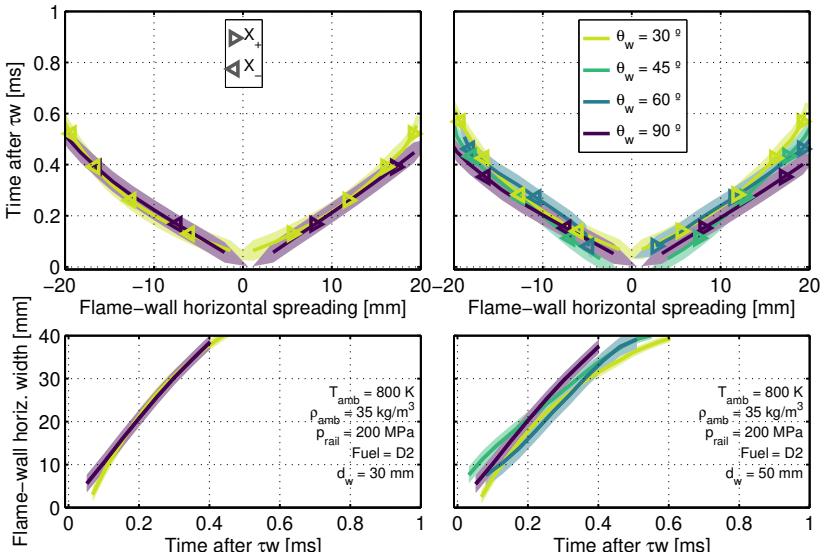

Figure 21: Flame horizontal spreadings and width varying wall angle (T_{amb} = 800 K; ρ_{amb} = 35 kg m^{-3}; p_{rail} = 200 MPa; Fuel = D2). Left: d_w = 30 mm. Right: d_w = 50 mm.

that the main cause of this *LoL* shortening at SWI conditions is the re-entrainment of hot gases that are products of combustion and that are entrained back into incoming fuel jet due to the wall curvature, which is not the case in the present research. It is important to highlight that the plotted lift-off results are the visible through lateral OH* chemiluminescence, which are the ones whose ignition delay is less susceptible to be affected by SWI.

As mentioned before, the employed OH* chemiluminescence optical setup is limited to obtain information for test points with lift-off lengths that are downstream from the flame thickness, and specially those whose *LoL* at free-jet conditions would surpass the wall location. Images from the frontal camera of the natural luminosity of the flame can be used to shed light on this regard. A sequence of images taken by the frontal camera through the wall for both wall angles 30° and 90° (fixing all the other operating and wall conditions), is shown in Figure 24. Free-jet tests at those operating conditions present a 32.79 mm lift-off length, while the wall has been located at 30 mm from the nozzle outlet in these samples. In contrast with Figure 5, where high-temperature and short-*LoL* conditions were set; there is a hole in the center of the flame footprint during the steady spreading along the wall, which means that SWI does not prevent the formation of a lift-off "length" downstream from the wall. This

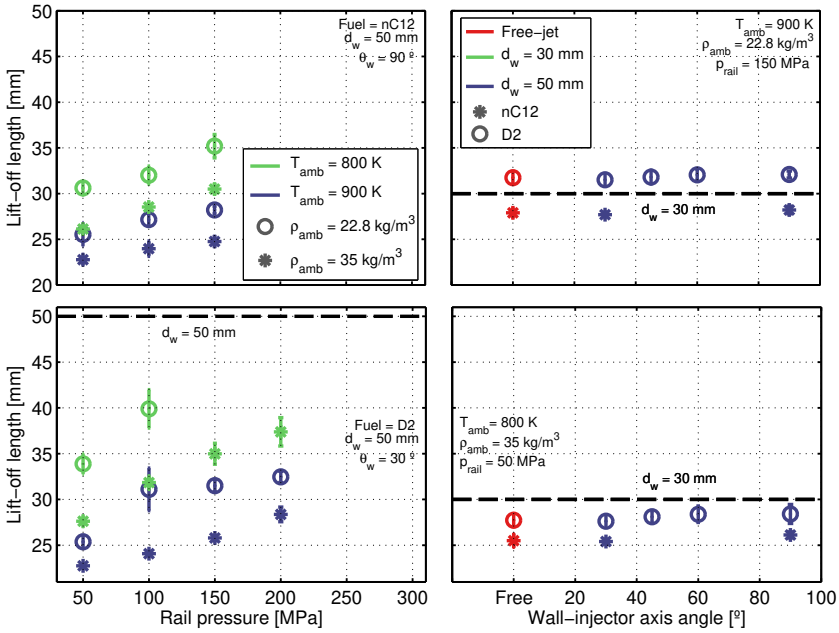

Figure 22: Lift-off length obtained for different parametric changes. Left set: *LoL* vs injection pressure varying ambient temperature and density. Right set: Variation of *LoL* vs. wall angle at different wall orientations and fuels (free-jet included). Please note that wall locations are shown in dashed black lines.

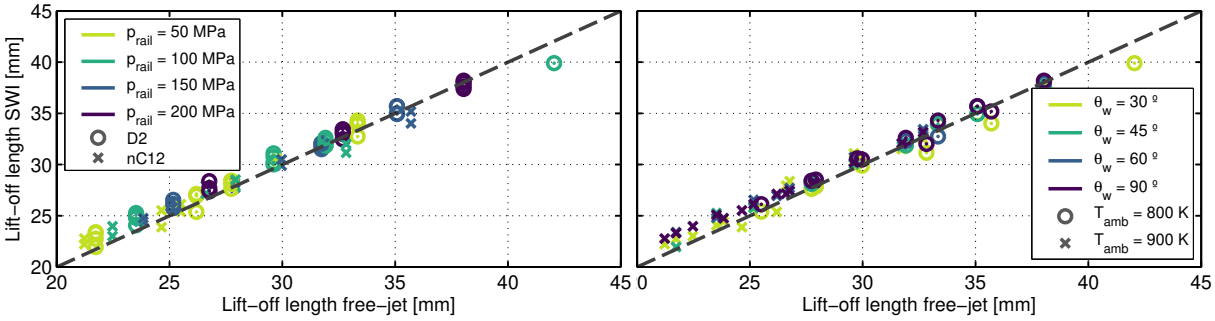

Figure 23: Lift-off length with the quartz wall in SWI conditions vs. ignition delay at free-jet conditions. The gray dashed line represents $ID_{free\text{-}jet} = ID_{SWI}$. Both plots have the same information differently classified. Left: Fuel and injection pressure variation. Right: Changes in wall position and gas temperature.

lift-off area appears onto the wall and its radial dimension is nearly constant until the end of the injection, as it happens with *LoL*.

With the purpose of estimating this zone expansion, an average image was created from the quasi-steady flame frames. Then, a threshold-based method has been applied (as done for spray or flame contour detection, but to detect dark zones in this case), and the central dark area has been numerically fitted to an ellipse. In inclined wall cases, the vertical projection of this area could present aberration due to the projection of the spray thickness, underestimating it. Therefore, the horizontal radius of the ellipse was the selected as a new metric for this "on-wall-lift-off", and it is referred hereinafter to as wall lift-off radius or $WLoR_{NL}$. The subscript is there to clarify that, in this article, images from natural luminosity were used to determine this dimension. However, it is important to highlight that this strategy aims to reach a qualitative link with the standard definition of lift-off length, but it is still not considered to be a robust quantitative variable due to the difference between both techniques in terms of different light filters and principles (lift-off length measured via OH* chemiluminescence). Changing this optical setup employing a frontal intensified camera would be a more consistent experimental methodology to estimate lift-off length spreading onto the wall. However, the approach presented in this article still shows interesting findings and allows to consistently compare $WLoR_{NL}$ at different operating and wall conditions.

Figure 25 depicts $WLoR_{NL}$ plotted against injection pressure, with variations in wall angle and ambient density.

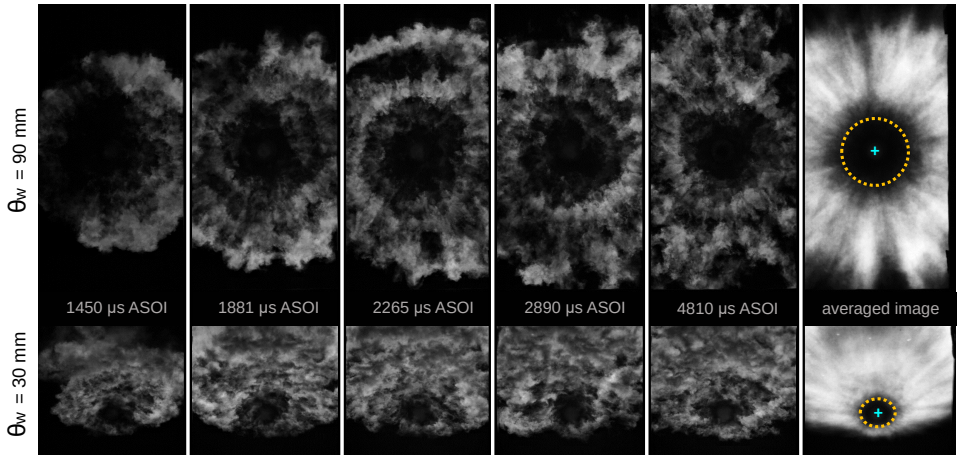

Figure 24: Sequence of the frontal SWI in raw images and definition of wall lift-off ratio $WLoR_{NL}$. (T_{amb} = 800 K; ρ_{amb} = 35 kg m^{-3}; p_{rail} = 100 MPa; d_w = 30 mm; θ_w = 90°; Fuel = D2). The image shows the flame at different times and finally, an average image of SWI phase.

There are not free-jet lift-off lengths in the test matrix that reached the 50 mm wall (the longest measured free *LoL* is 48.77 mm). The wall at 30° presents a shrunken area with a short $WLoR_{NL}$. Due to the flat wall, re-entrainment of hot combustion products showed to have no influence on visible *LoL*s. Nevertheless, the small scale of *WLoR* and the vicinity of the wall and this zone of reaction make that wall inclination in the bottom part, where an acute angle is formed between the wall and the original spray axis, acts like a curvature that promotes local hot gases entrainment and then, wall lift-off radius shortens. This significant effect of wall angle (a reduction up to 46 %) from a perpendicular wall to θ_w = 30°) is even stronger than the one produced by gas density and rail pressure, unlike the case of visible *LoL* that is not affected by the wall position. Even when $WLoR_{NL}$ is not strictly consistent with *LoL* due to their different optical techniques, it is interesting to notice how similar the trends are with ρ_{amb} and p_{rail} changes for both variables. Nonetheless, a further investigation with frontal visualization conducted via OH* chemiluminescence and a test plan with more points with large *LoL*s would allow not only to assess robust values of wall lift-off radius, but also to establish a relationship between visible *LoL* and *WLoR*. Based on the current methodology, it is observed that $WLoR_{NL} > LoL_{free} - d_w$, which suggests flame cooling with SWI, since the flame is at higher temperatures than the wall (which is nearly at T_{amb}) and the wall is a zone of no-mixing that prevents air entrainment in a significant portion of the spray surface area. Nevertheless, the improvement of the optical diagnostics and the use of the same techniques is still needed to establish a link between both views and to support this affirmation with proper quantitative certainty.

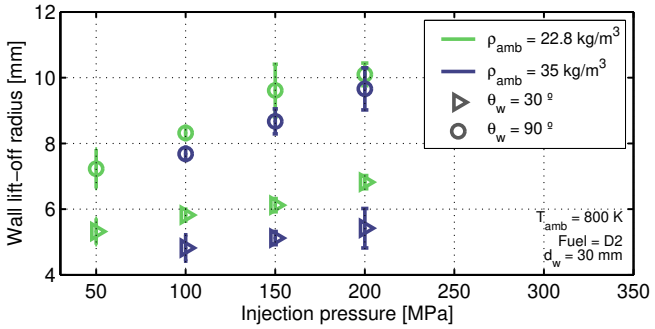

Figure 25: Wall lift-off ratio at different rail pressures, air density and wall angle. (T_{amb} = 800 K; d_w = 30 mm; Fuel = D2).

4. Conclusions

In this article, a simultaneous visualization with three cameras was performed to observe macroscopic characteristics of reacting sprays during SWI in terms of their vapor phase by the use of Schlieren imaging, of the soot-emitted light directly observed from the front and through the wall and the lift-off length detected via OH* chemiluminescence. A mono-orifice ECN injector with a heavy-duty-like diameter and *k-factor* $= 1.5$ has been employed, injecting both n-dodecane and commercial diesel in a combustion chamber of well-controlled ambient conditions and with a quartz wall with settable distance from the injector tip and inclination angle. Standard air was introduced into the chamber and oxygen concentration was nearly 21% for all the tests. The employment of a quartz wall not only allowed to record the flame from a frontal view, but also to keep the wall at a temperature similar to the one of the ambient and to reduce the thermal differences between the interaction of the spray with the wall and the one with the surrounding gases.

Ignition delay was calculated with the Schlieren images by the use of an intensity-based processing approach. Results showed that *ID* in SWI situation is similarly affected by parametrical changes as it is at free-jet conditions and wall angle effect showed to be negligible. Nevertheless, the change on spray morphology after spray collision and the increase of local turbulence levels improve air-fuel mixing and reduce *ID* for normally delayed ignition cases that are given on the wall and a reduction up to $15\,\%$ is observed with the quartz wall respect to free-jet tests.. In accordance with this, shorter ignition delays are found when the wall is closer to the injector tip. Spray spreading on the wall shows to be analogous respect to the known behavior of penetration for free reacting sprays, being affected by ignition delay in terms of both time of occurrence and premixing time. *R-parameter* follows five stages that have been recognized in free-jet literature: inert spray phase, ignition-induced peak, decelerating valley, momentum rise and a quasi-steady constant value that is higher than the inert one. Similarly, spray thickness onto the wall is affected by the combustion-driven expansion of the spray in an additive way respect to other parametrical variations that affect gas entrainment.

Horizontal spreading of the sooty flame onto the wall followed the same trends as the upwards spreading seen via Schlieren imaging, except that the reduced effect of inclination angle due to the variation on the measuring axis projection, which revealed that spreading dependency on wall angle is just given in the same direction of the inclination.

Finally and regarding the *LoL* analysis, short lift-off lengths that are visible with the intensified camera did not show variations produced by the wall respect to the free-jet case. However, the very flame thickness covered lift-off lengths that are close to the wall or on it. In this matter, frontal natural luminosity images are enlightening to visualize that the wall does not prevent lift-off length to grow, but it is still formed onto the wall in form of an elliptical hole on the flame footprint, which described in this document in terms of its horizontal radius as a new introduced variable that is referred to as wall lift-off radius or *WLoR*. This radius, measured from the images of natural luminosity, showed to be affected by ambient density and rail pressure changes in the same way lateral lift-off length is, but additionally it is largely reduced by wall inclination as a product of the promoted re-entrainment of burned products into the reaction zone. Also, the length of $WLoR_{NL}$ suggests a reduction in soot levels and the presence of spray cooling with the wall, due to its temperature close to the one of the ambient. However, these observations based on $WLoR_{NL}$ values need to be carefully considered and it is important to highlight that they are not entirely conclusive since optical techniques used in both frontal view and lift-off visualization are not consistent (OH* chemiluminescence vs. natural luminosity). An additional campaign with two intensified cameras to have frontal and lateral simultaneous visualization is recommended in order to shed light on the quantitative relationship between *LoL* and *WLoR*.

5. Acknowledgments

This research was funded by the Spanish Ministerio de Ciencias, Investigación y Universidades through project reference RTI2018-099706-B-I00. Part of the experimental hardware was purchased through funds obtained from Spanish Ministerio de Ciencia, Innovación y Universidades with FEDER funds through project with reference EQC2018-004605-P.

Finally, the support of Omar Huerta Cornejo and Borja Hurtado in conducting the experiments and laboratory work is greatly appreciated.

References

[1] S. Som, S. K. Aggarwal, Effects of primary breakup modeling on spray and combustion characteristics of compression ignition engines, Combustion and Flame 157 (2010) 1179–1193.

[2] M. Bardi, G. Bruneaux, L.-M. Malbec, Study of ECN Injectors' Behavior Repeatability with Focus on Aging Effect and Soot Fluctuations, SAE Technical Paper 2016-01-0845 (2016).

[3] R. Payri, F. J. Salvador, J. Gimeno, J. E. Peraza, Experimental study of the injection conditions influence over n-dodecane and diesel sprays with two ECN single-hole nozzles. Part II: Reactive atmosphere, Energy Conversion and Management 126 (2016) 1157–1167.

[4] M. Panão, A. L. N. Moreira, A systematic approach to model and interpret secondary atomization emerging from spray- wall impact in IC Engines, in: SPEIC14 - Towards Sustainable Combustion, Lisbon (Portugal), 2015.

[5] T. D. Fansler, M. F. Trujillo, E. W. Curtis, Spray-wall interactions in direct-injection engines: An introductory overview, International Journal of Engine Research 21 (2020) 241–247.

[6] L. M. Pickett, J. J. Lopez, Jet-wall interaction effects on diesel combustion and soot formation 2005 (2005).

[7] K. Ko, M. Arai, Diesel spray impinging on a flat wall, part i: Characteristics of adhered fuel film in an impingement diesel spray, Atomization and Sprays 12 (2002) 737–751.

[8] S. Y. Lee, S. U. Ryu, Recent progress of spray-wall interaction research, Journal of Mechanical Science and Technology 20 (2006) 1101–1117.

[9] J. Naber, R. Reitz, Modeling Engine Spray/Wall Impingement, SAE Technical Paper 880107 (1988).

[10] H. Kuniyoshi, H. Tanabe, G. T. Sato, H. Fujimoto, An Investigation on the characteristics of Diesel fuel spray, SAE Paper 800968 (1980).

[11] M. A. Gonzalez, G. L. Borman, R. D. Reitz, A Study of Diesel Cold Starting using both Cycle Analysis and Multidimensional Calculations, SAE Technical Paper 910180 (1991).

[12] L. Wachters, N. Westerling, The heat transfer from a hot wall to impinging water drops in the spheroidal state, Chemical Engineering Science 21 (1966) 1047 – 1056.

[13] V. Cole, D. Mehra, S. Lowry, D. Gray, A Numerical Spray Impingement Model Coupled With A Free Surface Film Model, in: The Fifth International Symposium on Diagonstics and Modeling of Combustion in Internal Combustion Engines, 2001.

[14] A. M. Lippert, D. W. Stanton, R. D. Reitz, C. J. Rutland, W. L. H. Hallett, Investigating the Effect of Spray Targeting and Impingement on Diesel Engine Cold Start, SAE Technical Paper 2000-01-0269 (2000).

[15] G. E. Cossali, A. Coghe, M. Marengo, The impact of a single drop on a wetted solid surface, Experiments in Fluids 22 (1997) 463–472.

[16] A. L. Yarin, D. A. Weiss, Impact of drops on solid surfaces: self-similar capillary waves, and splashing as a new type of kinematic discontinuity, Journal of Fluid Mechanics 283 (1995) 141–173.

[17] J. Naber, P. Farrell, Hydrodynamics of Droplet Impingement on a Heated Surface, SAE Technical Paper 930919 (1993).

[18] R.-h. Chen, L. C. Chow, J. E. Navedo, Optimal spray characteristics in water spray cooling, International Journal of Heat and Mass Transfer 47 (2004) 5095–5099.

[19] A. S. Moita, M. R. O. Panão, Advances and challenges in explaining fuel spray impingement : How much of single droplet impact research is useful ?, Progress in Energy and Combustion Science 36 (2010) 554–580.

[20] M. Panão, A. Moreira, Experimental study of the flow regimes resulting from the impact of an intermittent gasoline spray, Experiments in Fluids 37 (2004) 834–855.

[21] H. Pan, M. Xu, D. Hung, H. Lv, X. Dong, T. W. Kuo, R. O. Grover, S. E. Parrish, Experimental Investigation of Fuel Film Characteristics of Ethanol Impinging Spray at Ultra-Low Temperature, SAE Technical Paper 2017-01-0851 (2017).

[22] C. Arcoumanis, J. C. Chang, Heat transfer between a heated plate and an impinging transient diesel spray, Experiments in Fluids 16 (1993) 105–119.

[23] M. Z. Akop, Y. Zama, T. Furuhata, M. Arai, Characteristics of adhesion diesel fuel on an impingement disk wall part 1: Effect of impingement area and inclination angle of disk, Atomization and Sprays 23 (2013) 725–724.

[24] J. J. Lopez, L. M. Pickett, Jet/wall interaction effects on soot formation in a diesel fuel jet, International Symposium on Diagnostics and Modeling of Combustion in Internal Combustion Engines (COMODIA) (2004) 387–394.

[25] R. Payri, J. Gimeno, J. E. Peraza, T. Bazyn, Spray / wall interaction analysis on an ECN single-hole injector at diesel-like conditions through Schlieren visualization, Proc. 28th ILASS-Europe, Valencia (2017).

[26] C. Fan, D. Wang, K. Nishida, Y. Ogata, Visualization of diesel spray and combustion from lateral side of two-dimensional piston cavity in rapid compression and expansion machine, International Journal of Engine Research (2020) Published online.

[27] J. Gimeno, G. Bracho, P. Martí-Aldaraví, J. E. Peraza, Experimental study of the injection conditions influence over n-dodecane and diesel sprays with two ECN single-hole nozzles. Part I: Inert atmosphere, Energy Conversion and Management 126 (2016) 1146–1156.

[28] R. Payri, F. J. Salvador, J. Manin, A. Viera, Diesel ignition delay and lift-off length through different methodologies using a multi-hole injector, Applied Energy 162 (2016) 541–550.

[29] ECN, Engine Combustion Network, Online in http://www.sandia.gov/ecn/, 2010.

[30] M. Bardi, R. Payri, L.-M. Malbec, G. Bruneaux, L. M. Pickett, J. Manin, T. Bazyn, C. L. Genzale, Engine Combustion Network: Comparison of Spray Development, Vaporization, and Combustion in Different Combustion Vessels, Atomization and Sprays 22 (2012) 807–842.

[31] A. Pandal, J. Garcia-Oliver, J. Pastor, Eulerian cfd modeling of nozzle geometry effects on ecn spray a and d: assessment and analysis, International Journal of Engine Research 21 (2019) 73–88.

[32] R. Payri, J. Gimeno, J. Cuisano, J. Arco, Hydraulic characterization of diesel engine single-hole injectors, Fuel 180 (2016) 357–366.

[33] J. E. Peraza, F. Salvador, J. Gimeno, S. Ruiz, ECN Spray D visualization of the spray interaction with a transparent wall under engine-like conditions. Part I: Non-reactive impinging spray., Energy Conversion and Management XX (2020) XXX–XXX.

[34] R. Payri, J. P. Viera, Y. Pei, S. Som, Experimental and numerical study of lift-off length and ignition delay of a two-component diesel surrogate, Fuel 158 (2015) 957–967.

[35] J. Gimeno, P. Martí-Aldaraví, M. Carreres, J. E. Peraza, Effect of the nozzle holder on injected fuel temperature for experimental test rigs and its influence on diesel sprays, International Journal of Engine Research 19 (2018) 374–389.

[36] J. Benajes, R. Payri, M. Bardi, P. Martí-aldaraví, Experimental characterization of diesel ignition and lift-off length using a single-hole ECN injector, Applied Thermal Engineering 58 (2013) 554–563.

[37] F. R. Westlye, M. Battistoni, S. A. Skeen, J. Manin, L. M. Pickett, A. Ivarsson, Penetration and combustion characterization of cavitating and non-cavitating fuel injectors under diesel engine conditions, SAE Technical Paper 2016-01-0860 (2016) 15.

[38] D. L. Siebers, Liquid-Phase Fuel Penetration in Diesel Sprays, SAE Technical Paper 980809 (1998) 1–23.

[39] A. N. Lipatnikov, W. Y. Li, L. J. Jiang, S. S. Shy, Does Density Ratio Significantly Affect Turbulent Flame Speed?, Flow, Turbulence and Combustion 98 (2017) 1153–1172.

[40] J. M. Desantes, J. M. Garcia-Oliver, R. Novella, L. Pachano, A numerical study of the effect of nozzle diameter on diesel combustion ignition and flame stabilization, International Journal of Engine Research 21 (2020) 101–121.

[41] R. P. Fitzgerald, K. Svensson, G. Martin, Y. Qi, C. Koci, Early Investigation of Ducted Fuel Injection for Reducing Soot in Mixing-Controlled Diesel Flames, SAE Technical Paper 2018-01-0238 (2018) 1–17.

[42] A. M. Rusly, M. K. Le, S. Kook, E. R. Hawkes, The shortening of lift-off length associated with jet-wall and jet-jet interaction in a small-bore optical diesel engine, Fuel 125 (2014) 1–14.

[43] N. Maes, M. Hooglugt, N. Dam, B. Somers, G. Hardy, On the influence of wall distance and geometry for high-pressure n-dodecane spray flames in a constant-volume chamber, International Journal of Engine Research (2019).